Geotextiles and Geomembranes 45 (2017) 361–376

Contents lists available at ScienceDirect

Geotextiles and Geomembranes

journal homepage: www.elsevier.com/locate/geotexmem

An analytical solution for geotextile-wrapped soil based on insights from DEM analysis

Hongyang Cheng [a, b, *], Haruyuki Yamamoto [a], Klaus Thoeni [c], Yang Wu [d]

[a] Graduate School for International Development and Cooperation, Hiroshima University, 1-5-1, Kagamiyama, Higashi-hiroshima 739-8529, Japan
[b] Multi Scale Mechanics (MSM), Faculty of Engineering Technology, MESA+, University of Twente, P.O. Box 217, 7500 AE Enschede, The Netherlands
[c] Centre for Geotechnical and Materials Modelling, The University of Newcastle, Callaghan, NSW 2308, Australia
[d] Department of Civil and Environmental Engineering, Yamaguchi University, Tokiwadai 2-16-1, Ube 755-8611, Japan

ARTICLE INFO

Article history:
Received 31 May 2016
Received in revised form
20 April 2017
Accepted 29 April 2017
Available online 18 May 2017

Keywords:
Geosynthetics
Geotextile-wrapped soil
Discrete element method (DEM)
Stress path
Dilation rate
Uniaxial/triaxial compression test

ABSTRACT

This paper presents a novel analytical solution for geotextile-wrapped soil based on a comprehensive numerical analysis conducted using the discrete element method (DEM). By examining the soil–geotextile interface friction, principal stress distribution, and stress–strain relations of the constituent soil and geotextile in the DEM analysis, a complete picture of the mechanical characterization of geotextile-wrapped soil under uniaxial compression is first provided. With these new insights, key assumptions are verified and developed for the proposed analytical solution. In the DEM analysis, a near-failure state line that predicts stress ratios relative to the maximums at failure with respect to deviatoric strain is uniquely identified; dilation rates are found to be related to stress ratios via a single linear correlation regardless of the tensile stiffness of the geotextile. From these new findings, the assumptions on the stress-state evolution and the stress–dilatancy relation are developed accordingly, and the wrapped granular soil can therefore be modeled as a Mohr–Coulomb elastoplastic solid with evolving stress ratio and dilation rate. The development of the proposed analytical model also demonstrates an innovative approach to take advantage of multiscale insights for the analytical modeling of complex geomaterials. The analytical model is validated with the DEM simulation results of geotextile-wrapped soil under uniaxial compression, considering a wide range of geotextile tensile stiffnesses. To further examine the predictive capacity of the analytical model, the stress–strain response under triaxial compression conditions is solved analytically, taking both different confining pressures and geotextile tensile stiffnesses into account. Good agreement is obtained between the analytical and DEM solutions, which suggests that the key assumptions developed in the uniaxial compression conditions also remain valid for triaxial compression conditions.

1. Introduction

Geosynthetics are cost-effective and environmentally friendly geomaterials that can be designed with great flexibility to reinforce geostructures. Planar geosynthetic sheets, such as geotextiles and geogrids, are commonly embedded horizontally within retaining walls (Rowe and Skinner, 2001; Sukmak et al., 2016) and subgrades (Giroud and Han, 2004; Chen et al., 2015). The *2D circumferentially closed* cellular forms of geosynthetic reinforcements, e.g., geosynthetic encasements, are installed around cylindrical granular stone columns in soft foundations to improve the lateral support and restrain dilation (Pulko et al., 2011; Wu and Hong, 2014; Geng et al., 2017). Matsuoka and Liu (2003) proposed an earth-reinforcement method with *3D* complete encapsulations of soil, i.e., wrapping soils in *entirely closed* geotextile containers. The advantage of employing geotextile containers over lateral encasements lies in the tensile stresses developed along the additional hoop directions (transverse to the horizontal axes), which results in more confinement from both vertical and lateral directions in the wrapped soil. In practical applications, the geotextile containers are typically cuboidal shaped and fully filled with sands or gravels such

* Corresponding author. Multi Scale Mechanics (MSM), Faculty of Engineering Technology, MESA+, University of Twente, P.O. Box 217, 7500 AE Enschede, The Netherlands.
E-mail addresses: h.cheng@utwente.nl (H. Cheng), a040564@hiroshima-u.ac.jp (H. Yamamoto), klaus.thoeni@newcastle.edu.au (K. Thoeni), yangwu@yamaguchi-u.ac.jp (Y. Wu).

http://dx.doi.org/10.1016/j.geotexmem.2017.05.001
0266-1144/

that they can be easily stacked side by side into multiple layers as partial replacement of weak ground (Matsuoka and Liu, 2006) or as facings installed in front of geosynthetic-reinforced soil (GRS) retaining walls (Tatsuoka et al., 2007). Geotextile-wrapped soil (GWS), which incorporates the reinforcing mechanisms in both planar- and 2D cellular-form GRS, has been proven to be effective for constructing retaining structures (Wang et al., 2015), slope protections (Xu et al., 2008) and roads (Matsuoka et al., 2010), among others. Some authors have reported the application of GWS assemblies as damping layers to reduce traffic-induced vibrations (Muramatsu et al., 2009). Analogues to sand-filled geotextile containers are water/slurry-inflated geomembrane mattresses, which are typically stacked into offshore barriers. The analytical solutions proposed by Guo et al. (2014) can predict settlements of the mattresses and tensile force distributions on the mattress materials under pumping pressure. Nevertheless, the mechanical behavior of the semi-fluid materials that inflate the mattresses fundamentally differs from that of the granular soil wrapped within the containers. Moreover, the surcharge loads on sand-filled geotextile containers are generally considerably higher than those on water/slurry-inflated mattresses. Compared with conventional planar sheets, geosynthetics manufactured in circumferentially or entirely closed cellular forms produce greater improvement in the stiffness and strength of the soil (Latha and Murthy, 2007; Tafreshi and Dawson, 2010; Oliaei and Kouzegaran, 2017). However, the cellular forms inevitably complicate the constitutive behavior of the reinforced soil, making the analytical solution for this composite geomaterial a difficult task.

Some analytical solutions have been proposed for stone columns reinforced with circumferentially closed geosynthetic encasements in soft ground (Balaam and Booker, 1985; Pulko et al., 2011). The geosynthetic-encased stone columns were considered to be perfectly elastoplastic cylindrical solids in a triaxial state, whereas the surrounding soil was assumed to be elastic. The continuity of stress and strain was solved at the soil–stone interface, where the additional lateral pressure exerted by the encasement was taken into account. Rather than an elastoplastic approach, empirical relations, such as one between dilation rate and deviatoric strain, can be extracted from experimental results to develop a simplified solution (Wu and Hong, 2014). Matsuoka et al. (2004) adopted a similar method in deriving their analytical solution for GWS in cuboidal shapes. They approximated the evolution of stress ratio in GWS under uniaxial/triaxial compression using an exponential function of vertical strain. Although the empirical relation was calibrated by the test results of triaxial compression on the inside soil, the characterization of the stress states was incomplete: the lateral confining stresses in wrapped soil increase as the compression proceeds rather than remaining constant as in conventional triaxial tests. The assumption on the stress state was simplified in Tantono (2007), where stress ratios were set to constants and the values varied at different locations. Another major simplification in the existing analytical solutions (Matsuoka et al., 2004; Xu et al., 2008; Tantono, 2007) is that the volume of the wrapped soil during compression was assumed to be constant, whereas the dilation of GWS has been characterized as one of the key factors that contribute to the failure pattern in a recent discrete element method (DEM) analysis of sand-filled geotextile containers (Cheng et al., 2016).

The objective of this work is to examine existing assumptions and develop new ones for the analytical model of GWS (AN-GWS) with evidence provided by DEM simulations of the validated discrete element model of GWS (DE-GWS) and subsequently propose an elastoplastic analytical framework for this particular cellular-form of GRS. Based on new numerical insights obtained with the DE-GWS model previously validated by the authors, the assumptions for the AN-GWS model are made complete by including novel assumptions on stress path and dilation rate. Aided by these assumptions, a new elastoplastic formulation for the stress–strain behavior of GWS that satisfies the Mohr–Coulomb criterion is proposed. To the authors' knowledge, the present work is the first attempt to develop analytical solutions for the GWS material through an elastoplastic approach. The insights from the DEM analysis play an important role in this theoretical description, which fundamentally differs from the previous empirical solutions (Matsuoka et al., 2004; Xu et al., 2008; Tantono, 2007), where neither the evolution of the stress state nor the stress–strain behavior of the wrapped soil was taken into account. The remainder of this paper is organized as follows. Section 2 investigates the characteristics of the boundary and interface conditions of GWS under uniaxial and triaxial compression by using a previously calibrated and validated DE-GWS model (Cheng et al., 2016). The stress–strain responses of the constituent soil and geotextile are analyzed to facilitate the understanding of their respective behaviors and the correlations between them. Section 3 presents the new elastoplastic analytical solution. Section 4 discusses the validity of the model, and Section 5 examines the predictive capacity of the proposed analytical model in triaxial compression conditions.

2. DEM analysis of geotextile-wrapped soil

Numerical methods are generally adopted either to investigate the fundamental behaviors of geomaterials (Magnanimo and La Ragione, 2013; Kumar et al., 2014; Gu et al., 2017) or to predict the performance of complex geostructures (Thoeni et al., 2014; Hussein and Meguid, 2016; Effeindzourou et al., 2017). Although the finite element method provides reasonable predictions for geostructures with geosynthetic reinforcements in planar forms, numerous GRS-related works are conducted using the DEM. The majority of these works attempt to explore the reinforcement mechanisms of the GRS designed in various forms and shapes from a micromechanics perspective (Lai et al., 2014; Ngo et al., 2015; Bhandari et al., 2015; Wang et al., 2016). The knowledge accumulated from these works needs to be further exploited to facilitate the development of the analytical and constitutive modeling of GRS. To this end, the current work revisits some key findings (Section 2.2.2) obtained with the DE-GWS model of Cheng et al. (2016) and conducts a comprehensive analysis regarding the stress states and constitutive behaviors (Sections 2.2.1 and 2.3), through which the assumptions for the AN-GWS model are made complete with the newly established ones. In the following, the DEM fundamentals, i.e., contact laws and model representation, that govern the behavior of the DE-GWS model are introduced first. The evolution of interface friction as discussed in Cheng et al. (2016) is briefly addressed. Then, the distributions of principal stress during uniaxial and triaxial compression numerical tests are investigated in detail to verify the assumptions for the boundary conditions for the AN-GWS model. To acquire a complete picture of the GWS behaviors, the responses of the constituent soil and geotextile are presented considering a wide range of geotextile tensile stiffnesses: the constitutive behavior of the wrapped soil is presented in the $e-p'-q$ space, where e, p' and q correspond to void ratio, mean effective stress and deviatoric stress, respectively, and the average tensile stresses are correlated to the surcharge load.

2.1. A DEM model of geotextile-wrapped soil

The DE-GWS model was validated by comparing the numerical predictions with the experimental measurements of the stress–-strain responses of a sand-filled woven geotextile container (length

and width of 400 mm, height of 80 mm after initial compaction) subjected to uniaxial compression and simple shear (Cheng et al., 2016). As illustrated in Fig. 1 (a)–(b), the sand is represented by a particle packing assembled with 100 identical DEM representative volumes of Toyoura sand (coefficient of uniformity $C_u = 1.3$, average radius $\tilde{r} = 0.1$ mm). Each representative volume consists of 1000 particles whose radii are sampled from an upscaled particle size distribution of Toyoura sand ($\tilde{r} = 2.95$ mm). The representative volume was generated in periodic boundary conditions (Fig. 1(d)) and then calibrated with the triaxial response of a Toyoura sand specimen with an initial void ratio $e_0 = 0.68$. Readers are referred to Cheng et al. (2016) for details regarding the calibration. Because periodic boundary conditions were employed, the compatibility of the contact geometry and mechanics at the interfaces between neighboring representative volumes were guaranteed. The structural mechanics of the woven geotextile fabrics were approximated by a system of identical remote springs (Thoeni et al., 2013) linked with discrete spherical nodes positioned on an orthogonal mesh (Fig. 1(c)). The geotextiles are hence assumed to be isotropic for simplicity, despite the fact that they are typically anisotropic in reality. As shown in Fig. 1(b), the DE-GWS model was adapted in Cheng and Yamamoto (2016) to evaluate the performance of GWS and geosynthetic-layered soil under triaxial loading conditions. For clarity, only a half of the particle assembly that wraps the DE-GWS model within the periodic cell is illustrated in Fig. 1(b). Section 2.2 investigates polypropylene (PP) geotextile with a tensile strength of 31.2 kN/m because of its numerous applications in engineering practices in Japan (Cheng et al., 2013). The weak woven polyethylene (PE) geotextile with a tensile strength as low as 9 kN/m is also considered, although the material is not commonly applied in practice (Koerner, 2012), because it is the material that was used to validate the DEM model in Cheng et al. (2016). With both PE and PP geotextiles, a more comprehensive analysis can be conducted to seek key assumptions regarding the boundary and interface behaviors under uniaxial and triaxial compression (Fig. 1(a) and (b)). Section 2.3 encompasses four additional GWS cases, with the geotextile tensile stiffness set to half, two, three and four times that of the PP geotextile (denoted as 0.5PP, 2PP, 3PP and 4PP, respectively).

The simplified Hertz–Mindlin model (Thornton et al., 2011) is adopted for the relationship between contact forces and relative displacements of two adjoining particles. A Mohr–Coulomb-type plastic condition is enforced on the tangential force with contact friction angles to take sliding between particles and at particle–geosynthetic interfaces into account. The contact friction alone is insufficient to reproduce the exact macroscopic experimental response of dense sands (O'Sullivan, 2011). Therefore, moment transfer is enabled on the contact surfaces, where the moments and rotations are related via rolling and bending springs. To account for the nonlinear tensile behavior of both woven geotextiles, the internode remote springs (Fig. 1(c)) are defined using piecewise linear stress–strain relations, as shown in Fig. 2. Friction between wrap and weft was excluded for simplicity. Table 1 lists the micromechanical parameters that reproduce the triaxial response of Toyoura sand, as shown in Fig. 3. Note that these micromechanical parameters govern inter-particle or particle–geosynthetic contact behaviors and should thus not be interpreted as bulk properties, e.g., the 'contact' Young's moduli therein that appear to be extremely high in a macroscopic sense are used for computing contact stiffnesses in the normal and tangential directions according to the simplified Hertz–Mindlin model (Thornton et al.,

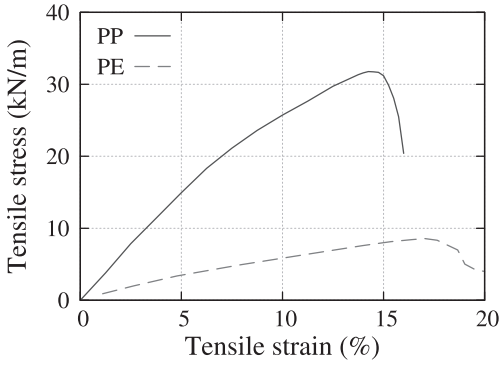

Fig. 2. Tensile stress–strain behavior of geotextile fabrics subjected to uniaxial tension. Piecewise linear approximation corresponds to input for the remote spring model.

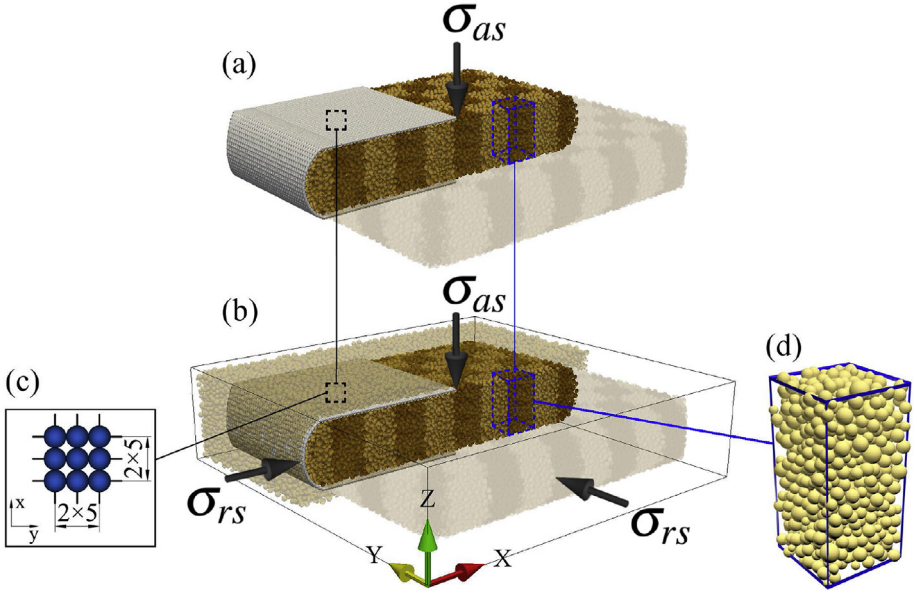

Fig. 1. DE-GWS model for (a) uniaxial compression and its adaptation for (b) triaxial compression, (c) discretization of geotextile fabrics and (d) representative volume of Toyoura sand. For clarity, only a quarter of the geotextile container is shown, and half of the particle packing is transparent.

Table 1
Micromechanical parameters for Hertz–Mindlin contact model in DEM analysis.

	Young's modulus (GPa)	Poisson's ratio	Rolling and twisting stiffness (Nm/rad)	Scaled density (10^3 kg/m^3)	Contact friction angle (°)
Soil particle	4	0.33	0.13	2650	29
Geotextile	8	0.33	0.13	444	21
Loading plate	200	0.33	0.13	7850	0

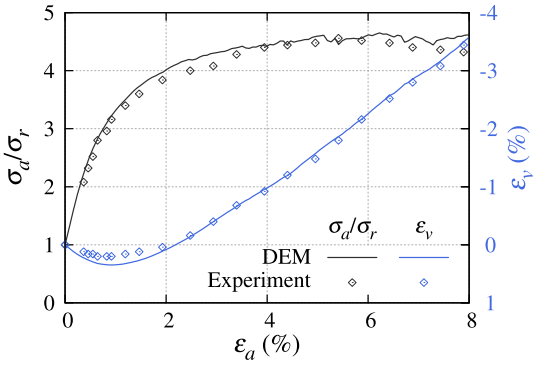

Fig. 3. Triaxial response of representative soil volume under 0.2 MPa confining pressure.

2011). Finally, the contact stiffness between two particles (i.e., soil–soil or soil–geotextile interaction) is calculated as the harmonic mean of the respective two values of each micromechanical parameters (e.g., Young's modulus).

After filtering the assembled particle packing with the assumed geometry of the geotextile container (Fig. 1(a)), the radii of the constituent particles were enlarged until the volume conformed to the boundary and the same void ratio as in the representative volume was obtained (Cheng et al., 2016). During generation of the model, virtual spherical nodes of the geotextile were fixed on the mesh, whereas in the uniaxial and triaxial loading stages, only the rotational degrees of freedom are blocked. To apply triaxial compression on GWS, the assembled particle packing was enclosed in a periodic cell (Fig. 1(b)) with particles of the same properties filling the remaining empty spaces. The void ratio of the GWS was measured from the total volume occupied by the assembled particle packing that represents the wrapped soil using a 3D Delaunay triangulation.

The following DEM analyses of the DE-GWS model under uniaxial and triaxial compression are conducted in a quasi-static manner using the open-source framework YADE (Šmilauer et al., 2015). Readers are referred to Cheng et al. (2016) and Cheng and Yamamoto (2016) for calibration and validation of the DE-GWS model under uniaxial and triaxial compression, whereas more details of the remote springs for modeling general tensile behavior can be found in Thoeni et al. (2013).

2.2. Characterization of stress state and interface behavior

2.2.1. Spatial distribution of principal stress

The average stress tensors are homogenized over the representative volumes using the Love–Weber formula. Fig. 4 illustrates the distribution of principal stress directions based on the homogenization performed over the representative volumes at different locations. Red, blue and green colors are used to render the scales of major, medium and minor principal stresses (σ_1, σ_2 and σ_3), respectively. The DE-GWS model involved in Fig. 4 considers PP geotextile and uniaxial compression conditions. As

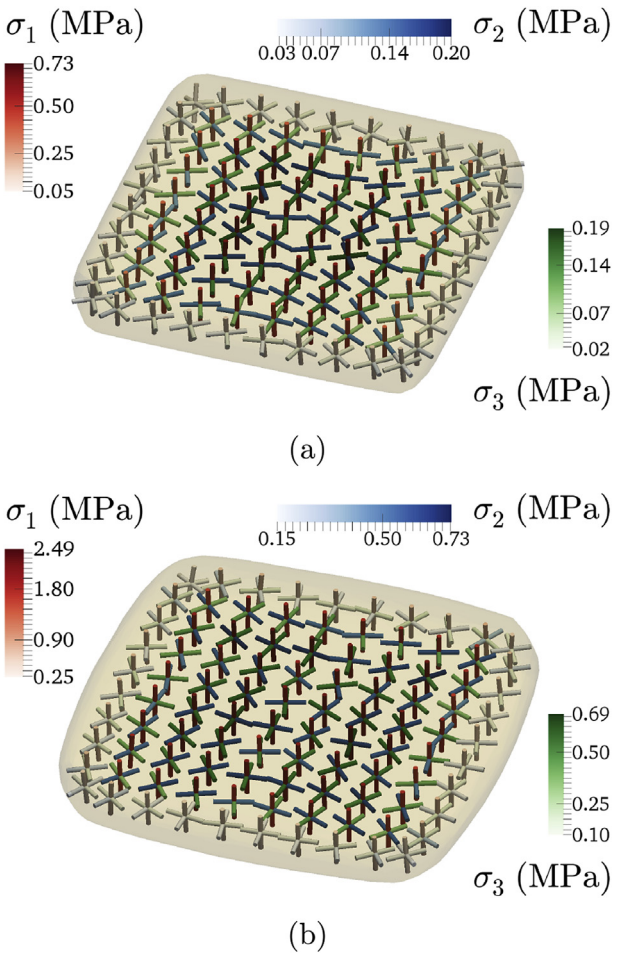

Fig. 4. Spatial distribution of principal stresses in GWS at (a) $e = e_{min}$ and (b) maximum σ_{am} states.

shown, the major principal stress directions remain parallel to the short axis z during the entire loading course, with σ_1 decreasing from the middle to the edges. Before the minimum void ratio e_{min} is reached, the majority of the medium and minor principal stress directions remain aligned with the long axes x and y, except for those around the corners, as shown in Fig. 4(a). As the compression proceeds, the medium principal stress directions become increasingly inclined to the $x = \pm y$ planes that lie perpendicular to the corner surface. The misalignment of the medium and minor principal stress directions propagates to the middle part when the GWS reaches its full strength, as shown in Fig. 4(b). The spatial distribution of principal stress directions presented here closely resembles that of a soil specimen in a cuboidal triaxial cell because stress concentration cannot be avoided at the cell corners. Nevertheless, the local misalignment of the medium and minor principal stress directions can be balanced by homogenizing the stresses over the entire GWS volume.

2.2.2. Interface friction

Considering the geotextile containers after compaction in engineering practices, the particle packing of the DE-GWS model is assumed to have a cuboidal shape with curved lateral surfaces and flat corners. A soil–geotextile interface friction coefficient can then be computed as the ratio of tangential to normal stresses homogenized over the bulk volume of a local particle assembly that is covered with the geotextile. To avoid the canceling out of asymmetric shear components, the homogenization is performed on a quarter of the GWS volume. As also shown by Cheng et al. (2016), friction is more significant on the lateral soil–geotextile interfaces (*yz*- and *zx*-planes) than on the horizontal interface (*xy*-plane) during triaxial compression. The friction angles on the lateral interfaces increase as the geotextile yarns progressively break, which is also true in the cases of drained triaxial compression (DTC, dashed lines), as shown in Fig. 5. Compared with the uniaxial compression (UC) cases (solid lines), the evolutions of interface frictions during drained triaxial compression are not stagnant in the pre-failure stage. This is because the geotextile fabrics at the initial stage of triaxial compression are not as strained as those under uniaxial compression.

In both the uniaxial and triaxial compression conditions, the maximum interface friction angles are considerably smaller than the interfacial shear strength measured in shear box tests, regardless of the tensile stiffness of the geotextile. This result can be attributed to compatible deformations at the soil–geotextile interfaces, where no shear stresses are produced. As long as the symmetry of the composite material remains intact, which means that no rupture of the fabrics occurs, interfacial shear should always be negligible compared with shear banding in the reinforced soil. Therefore, it is safe to assume smooth soil–geotextile interfaces for GWS under compression in the analytical framework presented in Section 3.

2.3. Behaviors of constituent materials

It is of vital importance to understand the behaviors of the constituent soil and geotextile of GWS in deriving the stress–strain solutions for GWS. The prediction of volumetric changes in the wrapped soil underpins the straining of geotextile fabrics, which in turn provides the soil with greater confinement and interlocking. Consequently, stress paths with distinctive features are experienced by the GWS. In addition to the soil behavior, this section attempts to relate the geotextile tensile response to the GWS bearing strength. A variety of tensile stiffnesses are thus considered to investigate their effects on the constitutive behavior of the wrapped soil and the bearing capacity of the GWS under uniaxial compression.

2.3.1. Constitutive relation of soil

Fig. 6(a)–(b) summarize the respective e–p' relations and stress paths of the reinforced soils wrapped with PE, 0.5PP, PP, 2PP, 3PP and 4PP geotextiles. Notably, the evolutions of void ratios in all cases initially follow the same compression line before dilation manifests, as shown in Fig. 6(a). One can observe that this compression line for GWS under uniaxial compression is of a similar shape as the normal compression line for sand (O'Sullivan, 2011). Fig. 6(b) verifies that the GWS stress paths consistently approach the nonlinear failure state line (FSL) of the Toyoura sand ($e_0 = 0.68$) independent of the tensile stiffness of the geotextile, which explains why all the e–p' curves initially follow the compression line (Fig. 6(a)). The failure principal stress ratio M_f on the FSL can be obtained from triaxial compression tests on the inside material (Sun et al., 2007). Fig. 6(c) presents the ratio between deviatoric stress q and mean effective stress p' evolving toward the failure state in a semi-log scale. After the failure state is reached, each p'–q/p' curve tends to align with the tangential direction along the FSL until the geotextile reinforcement begins to fail. The evolutions of the distances from the FSL to the p'–q/p' curves, termed the near-failure states in the following, are a family of parallel lines in the p'–$(M_f - q/p')$ plane. By replacing p' with the total deviatoric strain ε_d as the state variable, the near-failure state points in all cases collapse to a unique hyperbola, as shown in Fig. 7. Therefore, for uniaxial or triaxial compression, the predictions of q/p' can be obtained from the near-failure state line (NFSL) and the FSL without reference to the tensile stiffness of the geotextile.

2.3.2. Tensile response of geotextile fabrics

The effects of the physical properties (such as tensile stiffness and interface friction) and the forms of geosynthetic reinforcements on soil behavior have been demonstrated experimentally (Palmeira, 2009; Latha and Murthy, 2007; Tafreshi and Dawson, 2010), but their relationships are rarely discussed because of the versatility of geosynthetic reinforcements. Because this work focuses on the closed cellular form of geosynthetic reinforcements, the relationships between surcharge loads and geotextile tensile stresses during compression are investigated considering the aforementioned range of geotextile tensile stiffnesses. Fig. 8 shows the relationships between surcharge loads Q versus the tensile stresses averaged along two sets of geotextile hoops, i.e., t_{hr} (dashed lines) and t_{ha} (solid lines). *hr* and *ha* represent the hoops in the vertical and horizontal planes perpendicular to the lateral and vertical axes, respectively, as shown in Fig. 9. To better illustrate the tension–load relations, both the loads and the average tensile stresses are scaled with respect to the respective maximums of Q, t_{hr} and t_{ha} obtained in the PP case.

Fig. 8 reveals linear relationships between the tensile stresses and the surcharge loads before the geotextile fabrics are strained to

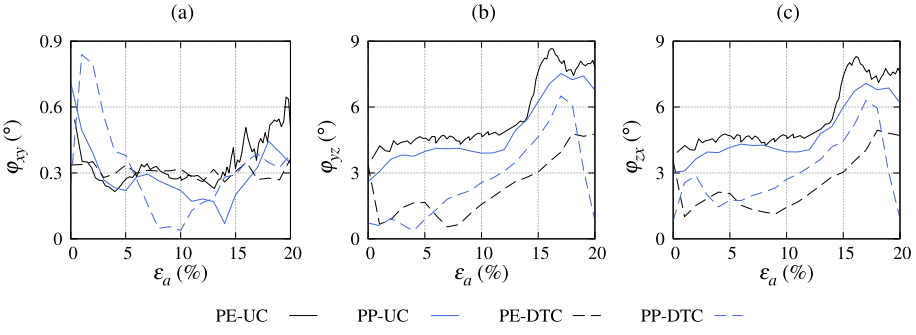

Fig. 5. Evolution of interface friction angles between soil and geotextile in (a) *xy*-, (b) *yz*- and (c) *zx*-planes.

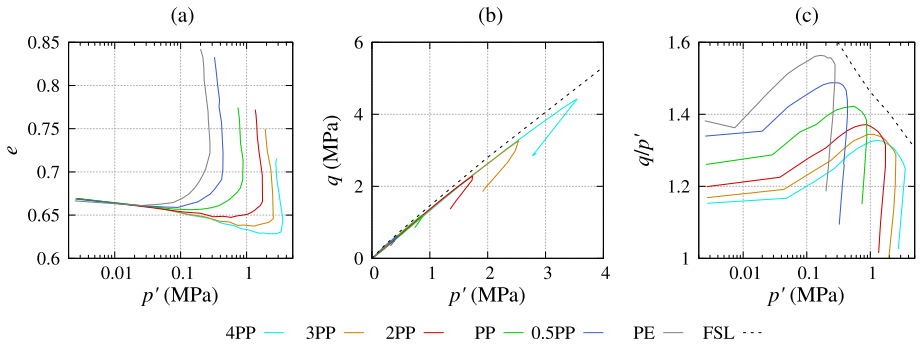

Fig. 6. Constitutive behaviors of wrapped soil in (a) p'–e and (b) p'–q planes, and (c) evolution of stress ratio q/p' versus mean stress p'.

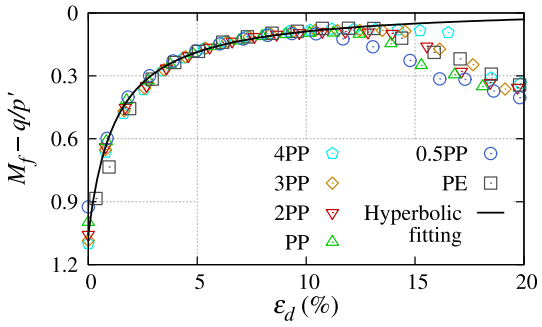

Fig. 7. Unique near-failure state line in ε_d–$(M_f - q/p')$ plane for GWS simulations with different geotextiles.

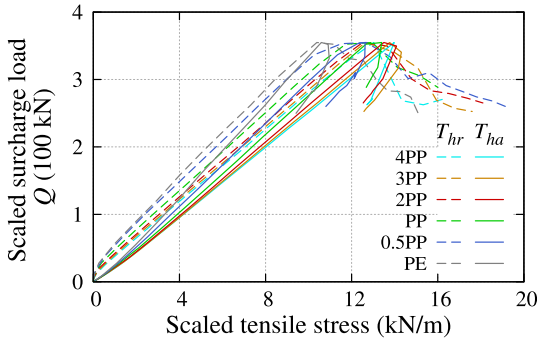

Fig. 8. Tensile stress–axial load relationships scaled to the PP case.

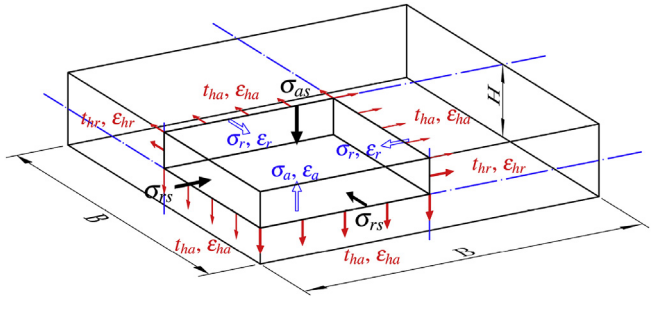

Fig. 9. Schematic illustration of stresses and strains in the analytical model of geotextile-wrapped soil.

failure. The evolutions of the scaled Q with respect to the scaled t_{hr} and t_{ha} lie very close to each other despite the difference in the geotextile tensile stiffness and the hoop directions. The above findings together with the principal stress ratio in the wrapped soil as a function of ε_d and p' suggest that the tensile stiffness of the wrapping geotextile has no impact on the relative values for the stresses within the soil and the geotextile under compression. Because the confinement from the geotextile encapsulation is the only external load on the soil, the ratio between the additional vertical and lateral confining pressures is also deemed to be independent of the tensile stiffness. Nevertheless, the stress magnitudes and ultimate bearing capacity during compression are apparently affected by the geotextile tensile stiffness, as demonstrated in Fig. 6(b). It appears that the influence of this factor can be accounted for by a reasonable value for the Young's modulus of GWS.

3. An analytical model for geotextile-wrapped soil

As observed in experiments (Cheng et al., 2013) and DEM simulations of uniaxial/triaxial compression (Cheng et al., 2016; Cheng and Yamamoto, 2016), the sand-filled cuboidal geotextile container (length $B = 400$ mm and height $H = 80$ mm after initial compaction) does not possess severely bulged lateral surfaces until the geotextile fabrics begin to fail. Therefore, there is no need for a rigorous description of the container shape, as performed by Guo et al. (2014). A cuboid should work properly as the assumed geometry for the analytical model of the wrapped soil and the geotextile encapsulation. Fig. 9 illustrates the external stresses σ_{as} and σ_{rs} applied from the vertical and lateral directions on the geotextile encapsulation and those produced within the wrapped soil σ_a and σ_r. The equilibrium condition is satisfied by the tensile stresses and the external and internal confining stresses, as shown in Fig. 9. With the new insights obtained from the DEM analysis in Section 2.3, the following fundamental assumptions are taken into account to facilitate the development of the analytical solution for GWS under compression:

(1) Stress state and boundary conditions:
   a. The principal directions of the internal stresses within the wrapped soil are aligned with the vertical and lateral axes, neglecting the corner effect and interface friction.
   b. The internal stresses produced in the wrapped soil are uniformly distributed on all faces of the cuboidal analytical model.

(2) Soil behavior:
   a. The initial contraction of the wrapped soil follows the compression line in the semi-log p'–e plane regardless of the tensile stiffness of the geotextile.
   b. The principal stress ratio is predicted by a unique near-failure state line that describes the principal stress ratio

converging to the failure state with respect to deviatoric strain.

c. The plastic behavior of the wrapped soil is governed by the Mohr–Coulomb yield criterion with an evolving dilation rate related to the principal stress ratio.

(3) Geotextile behavior:

a. The evolutions of the average tensile stresses and strains are the same along the hoops in the horizontal and vertical planes.

b. The geotextile behaves as a perfectly elastic material with the same tensile stiffness for every constituent hoop of the geotextile container.

3.1. A general framework for stress–strain relation under compression

In the case of geosynthetic-encased stone columns, additional lateral confinements are provided by the circumferential hoops in the horizontal plane. The equilibrium conditions for the surrounding soil, stone columns and encasement are satisfied at the soil–column interfaces, where the radial stress difference is taken by the geosynthetic encasement accordingly. In addition to the confinements from circumferential hoops, the GWS-type cellular reinforcement introduces two additional sets of hoops in the lateral planes. Consequently, both the vertical and lateral confinements are largely enhanced by the additional planar reinforcements (Cheng and Yamamoto, 2016). Note that the analytical solutions for the stone columns (Pulko et al., 2011; Balaam and Booker, 1985) require the same fundamental assumptions as the present analytical model, e.g., triaxial stress state and negligible interfacial shear. Analogous to the encased stone columns, the equilibrium equations of the wrapped soil can be expressed considering all the stresses and strains depicted schematically in Fig. 9. It follows:

$$\sigma_{as}B^2(1-\varepsilon_r)^2 + 4Bt_{hr}(1-\varepsilon_{ha}) = \sigma_a B^2(1-\varepsilon_r)^2 \tag{1}$$

$$\sigma_{rs}BH(1-\varepsilon_r)(1-\varepsilon_a) + t_{ha}(2B+2H)(1-\varepsilon_{hr}) = \sigma_r BH(1-\varepsilon_r)(1-\varepsilon_a) \tag{2}$$

where the average tensile strains ε_{ha} and ε_{hr} are linearly related to their respective stresses via the geotextile tensile stiffness J, which is assumed as a material constant. The initial length B and height H of the cuboidal model are assumed to be 400 mm and 80 mm, respectively, due to the negligible bulged lateral surfaces. In light of assumption 3(a) pertaining to the tensile stress distribution along the hoops, the subscripts ha and hr are reduced to h, which denotes the tensile stress/strain along any hoop direction. Additionally, note that relative movements at the soil–geotextile interfaces are allowed because of the approximation of the shape of the container using a cuboid. Hence, the elongations of the hoops ε_{ha} and ε_{hr} are assumed to be independent of the vertical and lateral strains ε_a and ε_r.

The expression for the surcharge σ_{as} as a function of the internal stresses and strains within the wrapped soil under uniaxial/triaxial compression reads as

$$\sigma_{as} = K\sigma_r - \frac{2(\sigma_r - \sigma_{rs})(H/B)(1-\varepsilon_a)}{(H/B+1)(1-\varepsilon_r)} \tag{3}$$

where $K = \sigma_a/\sigma_r$ is the principal stress ratio within the wrapped soil domain, which can be derived from q/p'. As stated in Section 2.3.1, q/p' can be calculated as the failure stress ratio M_f subtracted from the corresponding near-failure state variable $M_f - q/p'$ at the same p' and ε_d. The unique correlation between this new state variable $M_f - q/p'$ and ε_d, as shown in Fig. 7, can be formulated in a hyperbolic equation such as

$$M_f - q/p' = \frac{\kappa}{\varepsilon_d + \lambda} - \xi \tag{4}$$

with the corresponding parameters κ, λ and ξ listed in Table 2. The FSL that the stress paths in Fig. 6(b) are approaching is identical to the FSL of Toyoura sand ($e_0 = 0.68$). Hence, the following equations obtained from triaxial compression tests on Toyoura sand specimens (Yao et al., 2008; Wu et al., 2013, 2014) can also be employed in the current analytical model of GWS:

$$M_f = q_f \Big/ p' = M(p'/p_c)^{-n} \tag{5}$$

where the parameters M, n and p_c used by Yao et al. (2008) are listed in Table 2.

Eq. (2) presents the general framework of the analytical solution for GWS under compression. It is not surprising that the terms involved with tensile stresses/strains are canceled out in Eq. (3). This is considered reasonable because the tensile stiffness of the geotextile J has a marginal effect on the ratios among σ_a, σ_r, and σ_{as}, as shown in Figs. 6(b) and Fig. 8. To solve ε_a, ε_r and ε_h for a given surcharge history with Eq. (3), a suitable analytical model is required to express the strains in terms of the internal stresses produced by the wrapped soil. Hence, the total strain tensor $\boldsymbol{\varepsilon}$ is decomposed into an elastic and a plastic part, i.e., $\boldsymbol{\varepsilon} = \boldsymbol{\varepsilon}^e + \boldsymbol{\varepsilon}^p$. Each part is calculated with the respective stress–strain relation that characterizes the contractive or dilative behavior of GWS, respectively.

3.2. Initial elastic response

The evolution of void ratio initially following the compression line in Fig. 6(a) provides a basis for predicting the volumetric strain ε_v of GWS. Fig. 10 is produced by re-plotting the data in Fig. 6(a) on the ε_v–$(p'/p_a)^{0.3}$ plane, as performed by Yao et al. (2008) for sand in normal compression. The dilation parts are omitted to better illustrate the correlation. A unique straight line is thus identified, to which the state points of all six simulations collapse. This linear relationship facilitates the prediction of the initial ε_v without special consideration given to the tensile stiffness of the geotextile. The contractive ε_v produced in GWS under the compression is assumed to be elastic/elastoplastic, as in most constitutive models of sand. The remaining plastic part is considered within the incremental stress–strain relationship for a Mohr–Coulomb elastoplastic material. Although deviatoric strain is generally assumed to occur only in the plastic deformation regime, the current AN-GWS model allows for an elastic deviatoric strain ε_d^e to be produced during compression. Hence, using the same expression as for the normal compression line for sand (Yao et al., 2008; Wu et al., 2013, 2014), the elastic volumetric and deviatoric strains ε_v^e and ε_d^e can be directly predicted from p' by

$$\varepsilon_v^e = C_t\left[(p'/p_a)^m - (p_0'/p_a)^m\right] \tag{6}$$

where m is a material constant, which equals 0.3 for sand; p_a is the atmospheric pressure ($p_a = 0.1$ MPa); and the values of the compression index C_t and the initial mean stress p_0' are obtained from the slope and intercept of the straight line in Fig. 10.

Table 2
Parameters of the proposed analytical solution for geotextile-wrapped soil.

Compression line	Failure state line (FSL)	Near-failure state line (NFSL)	Stress–dilatancy relation	Young's modulus estimation
$C_t = 1.372$	$M = 1.35$	$\kappa = 1.386$	$p_1 = 1.68$	$\alpha = 26.1$
$m = 0.3$	$n = 0.0723$	$\lambda = 1.27$	$p_2 = 0.344$	$\beta = 0.74$
$p_a = 0.1$ MPa	$p_c = 3.255$ MPa	$\xi = 0.035$		
$p_0 = 2.6$ kPa				

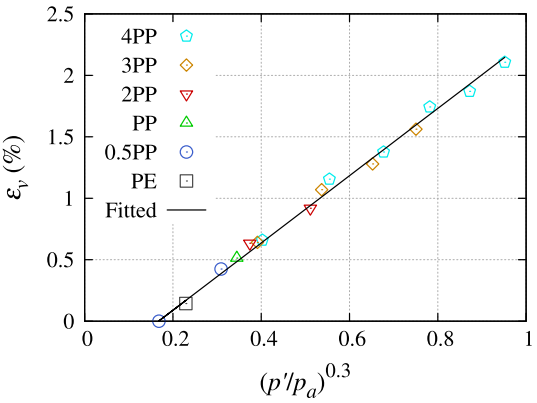

Fig. 10. Evolution of volumetric strain versus $(p'/p_a)^{0.3}$ before dilation occurs and the fitted compression line.

$$\varepsilon_d^e = \frac{2q(1+\upsilon)}{9p'(1-2\upsilon)}\varepsilon_v^e \tag{7}$$

where υ is the Poisson's ratio of the wrapped soil and q/p' is predicted from p' on the FSL and NFSL, which is the newly recognized state line for GWS-type reinforced sands. Note that the fitted value for p_0', 2.6 kPa in the case of GWS, is very close to the mean effective stress in the unreinforced sand at the passive failure condition ($K_p = 5.25$) under a $\sigma_{as,0} = 5.635$ kPa surcharge. The same level of surcharge was applied as the initial compaction on the sand-filled geotextile container in the DEM and experimental uniaxial compression tests (Cheng et al., 2016). Therefore, it is postulated that the additional confining pressure from the geotextile encapsulation is negligible at the initial loading stage. Note that the value of C_t given in Table 2 for the GWS is larger than 0.84 for Toyoura sand obtained from isotropic compression tests (Yao et al., 2008). This difference could possibly be caused by the initial anisotropic stress and fabric states in the wrapped soil.

3.3. Incremental plastic response

With the elastic strains predicted by Eqs. (6) and (7), the plastic stress–strain behavior of GWS remains to be solved by an analytical model that can consider the dilatancy of soil. According to Balaam and Booker (1985) and Pulko et al. (2011), a simplified solution can be obtained by assuming that the stone columns are kept at triaxial stress states during compression. It can be understood from the previous DEM analysis (Section 2.3.1) that the behavior of GWS satisfies the same assumptions applied in the analytical solution for the stone columns with geosynthetic encasement. Under uniaxial and triaxial compression, these two geomaterials are expected to undergo significant plastic dilation, which in turn facilitates the confinement effect. The wrapped/encased geomaterials can be considered to be perfectly elastoplastic solids that satisfy the Mohr–Coulomb yield criterion. The plastic stress–strain relationship is written incrementally as

$$\begin{Bmatrix} \mathrm{d}\sigma_a^p \\ \mathrm{d}\sigma_r^p \end{Bmatrix} = D\begin{bmatrix} K_\psi K' & 2K' \\ K_\psi & 2 \end{bmatrix}\begin{Bmatrix} \mathrm{d}\varepsilon_a^p \\ \mathrm{d}\varepsilon_r^p \end{Bmatrix} \tag{8}$$

where $\mathrm{d}\sigma_a^p$ and $\mathrm{d}\sigma_r^p$ are the vertical and lateral stress increments that produce the corresponding strain increments denoted as $\mathrm{d}\varepsilon_a^p$ and $\mathrm{d}\varepsilon_r^p$, respectively. The incremental stresses and strains are correlated via the material parameter D, the stress increment ratio K' and the strain increment ratio K_ψ, which are respectively defined by

$$D = \frac{E}{2 + K_\psi K' - 2\upsilon\left(1 + K_\psi + K'\right)} \tag{9}$$

$$K' = \frac{\mathrm{d}\sigma_a^p}{\mathrm{d}\sigma_r^p} = \frac{1+\sin\varphi}{1-\sin\varphi} = \frac{2\mathrm{d}q/\mathrm{d}p' + 3}{-\mathrm{d}q/\mathrm{d}p' + 3} \tag{10}$$

$$K_\psi = \frac{\mathrm{d}\varepsilon_r^p}{\mathrm{d}\varepsilon_a^p} = \frac{1+\sin\psi}{1-\sin\psi} = \frac{2\mathrm{d}\varepsilon_v^p/\mathrm{d}\varepsilon_d^p - 3}{2\mathrm{d}\varepsilon_v^p/\mathrm{d}\varepsilon_d^p + 6} \tag{11}$$

where φ is the peak friction angle, ψ is the dilation angle, and E is the Young's modulus of the reinforced geomaterial. In the original work of Balaam and Booker (1985), φ and ψ are assumed to be constant, which is not necessarily true for reinforced geomaterials due to their nonlinear nature, e.g., a nonlinear failure state line.

3.3.1. Prediction of principal stress and strain ratios

In the case of the geotextile-wrapped Toyoura sand, K' is calculated as the tangent of the nonlinear stress path such as those in Fig. 6(b). It was demonstrated in Section 2.3.1 that the principal stress ratio of GWS under uniaxial compression can be obtained from the near-failure and failure states associated with the total deviatoric strain and the mean stress. Therefore, K' can readily be derived from the ratio of principal stress increments $\mathrm{d}q/\mathrm{d}p'$ via Eq. (10), regardless of the tensile stiffness of the geotextile.

The validated discrete element model (Cheng et al., 2016) offers thorough measures of key variables that are otherwise difficult to acquire in conventional laboratory tests, such as q/p' and $\mathrm{d}\varepsilon_v^p/\mathrm{d}\varepsilon_d^p$ in wrapped soil. Fig. 11 plots the relationships between q/p' and dilation rate $-\mathrm{d}\varepsilon_v^p/\mathrm{d}\varepsilon_d^p$ obtained from the six DEM simulations with various geotextile tensile stiffnesses. The post-failure parts are excluded in Fig. 11 for clarity. It can be observed that the origins of all the $-\mathrm{d}\varepsilon_v^p/\mathrm{d}\varepsilon_d^p$–$q/p'$ curves are apparently aligned along a unique straight line (solid black line). As $-\mathrm{d}\varepsilon_v^p/\mathrm{d}\varepsilon_d^p$ increases, the rates of increase in q/p' reduce in all six simulations, approaching their respective plateaus. Note that the scattered data for the DEM simulations with different J are aligned parallel to each other. This tendency is more pronounced in Fig. 6(b) and the q/p'–ε_d curves that are omitted due to the indirect contribution to the new assumptions. This key finding indicates that the relationship between stress ratio and dilation rate should be related only to one variable that differs among all the simulation cases, i.e., the geotextile tensile stiffness J. Therefore, rather than employing a hardening law

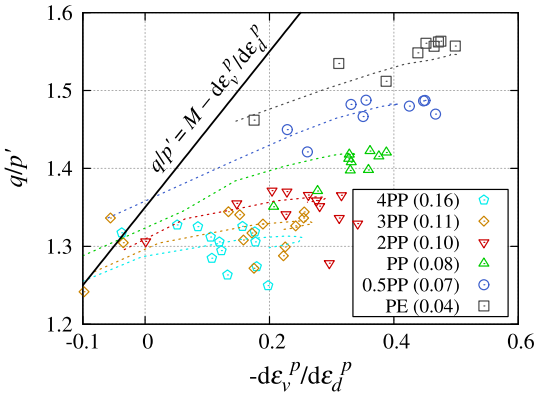

Fig. 11. Stress–dilatancy relations for granular soil wrapped with different geotextiles predicted from the DEM simulations (markers) and the analytical model (dashed lines). Numbers in parentheses correspond to the RMSEs between analytical and DEM results for the respective geotextile cases.

applicable for all the GWS cases with different J, the present work assumes the stress paths to be strictly governed by ε_d (Eq. (4)) and p' (Eq. (5)). More importantly, without a cap yield surface, an empirical stress–dilatancy rule needs to be enforced on the Mohr–Coulomb model for the prediction of K_ψ or $-\mathrm{d}\varepsilon_v^p/\mathrm{d}\varepsilon_d^p$.

Considering the straight line described by $q/p' = M - \mathrm{d}\varepsilon_v^p/\mathrm{d}\varepsilon_d^p$ as in the original Cam-clay model, the reference states can be defined for the stress–dilatancy relations of GWS with the stress ratio at failure $M_f = q_f/p'$ and the corresponding dilation rate $D_f^p = (-\mathrm{d}\varepsilon_v^p/\mathrm{d}\varepsilon_d^p)_f = M_f - M$. Similar to how the near-failure stress states are defined in Fig. 7, both the stress ratios and dilation rates in each simulation case are regulated with respect to the reference states M_f and D_f^p produced at the same ε_d and p', as shown in Fig. 12. It appears that all the regulated state points are located near a straight line in the $(D_f^p + \mathrm{d}\varepsilon_v^p/\mathrm{d}\varepsilon_d^p)$–$(M_f - q/p')$ plane. Therefore, the dilation rate $-\mathrm{d}\varepsilon_v^p/\mathrm{d}\varepsilon_d^p$ can be predicted using $M_f - q/p'$ (Eq. (4)) through a linear correlation:

$$-\mathrm{d}\varepsilon_v^p \Big/ \mathrm{d}\varepsilon_d^p = D_f^p - \left[p_1\left(M_f - q/p'\right) - p_2\right] \tag{12}$$

with the parameters p_1 and p_2 given in Table 2. As shown in Fig. 11, good agreement is obtained between the predicted stress–dilatancy relations and the measurements obtained from the DEM simulations of GWS considering different geotextile tensile stiffnesses. With these new assumptions for the evolutions of stress ratio (Eq. (5)) and dilation rate (Eq. (12)), material nonlinearity is introduced in the analytical model.

3.3.2. Relationship between tensile stiffness of geotextile and Young's modulus of wrapped soil

As discussed above, the parallel-aligned fitted curves in Fig. 11 suggest that the tensile stiffness of the geotextile plays a key role in the stress–strain behavior of the wrapped soil. In addition, it was found in Section 2.3.2 that the tensile stiffness of the geotextile appears to affect only the stress level, not the ratios among stress components. Hence, it is reasonable to take the influence of the tensile stiffness of the geotextile within the Young's modulus of the wrapped soil into account. Writing the stress increments in terms of $\mathrm{d}p'$ and K' and substituting Eq. (9) for D in Eq. (8) results in the following plastic stress–strain relation:

$$\mathrm{d}\varepsilon_a^p = \frac{\mathrm{d}\varepsilon_r^p}{K_\psi} = \frac{1}{E}\mathrm{d}p^* \tag{13}$$

with

$$\mathrm{d}p^* = \frac{2 + K_\psi K' - 2\upsilon\left(1 + K_\psi + K'\right)}{K_\psi(K' + 2)}\mathrm{d}p' \tag{14}$$

where the material parameters K' and K_ψ are calculated from $\mathrm{d}q/\mathrm{d}p'$ and $\mathrm{d}\varepsilon_v^p/\mathrm{d}\varepsilon_d^p$ via Eqs. (10) and (11). Plotting $\mathrm{d}\varepsilon_a^p$ against the generalized mean stress increment $\mathrm{d}p^*$ defined by Eq. (14) presents a group of linear relationships, as shown in Fig. 13. These measurements obtained from the DEM simulations in Fig. 13 further confirm the validity of applying Eq. (13) for the dilative behavior of GWS-type reinforced geomaterials. Fig. 14 plots the slope of the straight line in each simulation case against the corresponding geotextile tensile stiffness. A clear power-law relation $E = \alpha J^\beta$ is identified between the tensile stiffness of the geotextile (10^3 kN/m) and the Young's modulus of wrapped soil (MPa). The material constants α and β are listed in Table 2.

3.4. Complete elastoplastic solution for geotextile-wrapped soil

The complete stress–strain response of the GWS under compression loading conditions is obtained using its contractive and dilative parts computed in Eqs. (6), (7) and (13). The contractive volumetric strain of GWS ε_v^e is assumed to be elastic; thus, it can be predicted from the compression line upon a given mean stress (Eq. (6)). The elastic deviatoric strain ε_d^e is introduced (Eq. (7)) in

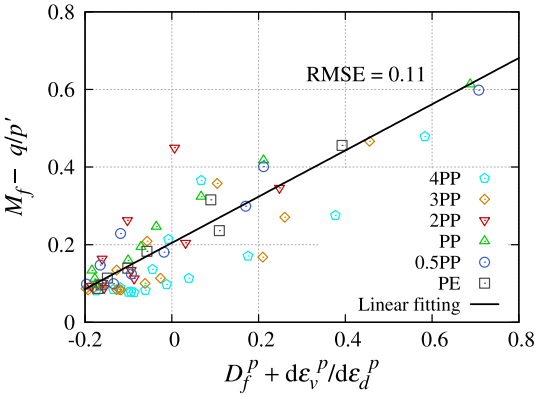

Fig. 12. Unique relationship between the relative states of principal stress ratio and dilation rate with respect to their failure values. The RMSE is measured between the analytical and DEM results taking all geotextile cases into account.

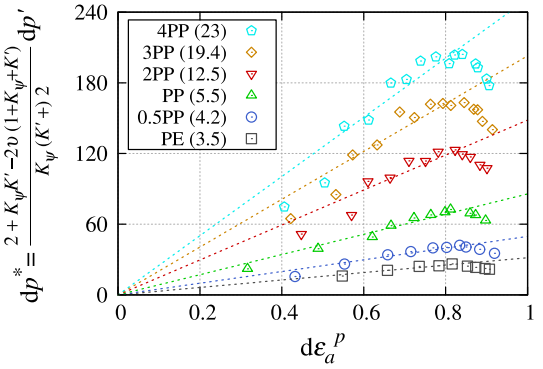

Fig. 13. Relationships between plastic vertical strain increment and generalized mean stress increment measured in the DEM simulations (markers) and predicted by the analytical model (dashed lines). Numbers in parentheses correspond to the RMSEs between the analytical and DEM results for the respective geotextile cases.

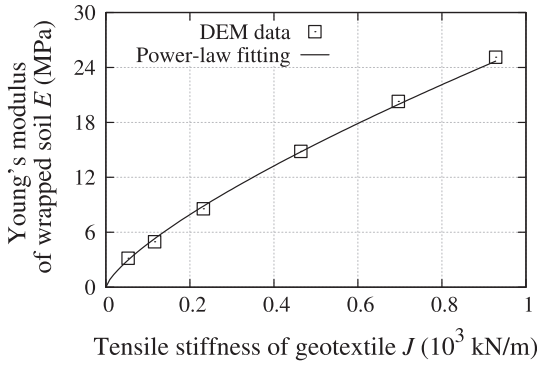

Fig. 14. Empirical relationship between the tensile stiffness of geotextile and Young's modulus of wrapped soil.

addition to ε_v^e, which differs from the assumption for deviatoric strain in some constitutive models. Nevertheless, the measurements of plastic strain increments, with ε_d^e excluded, show a linear correlation with the generalized mean stress (Fig. 13), as suggested in Eq. (13). The good agreement verifies the validity of assuming deviatoric strain in the elastic deformation regime. Therefore, the feasibility of adapting the plastic solution for the encased stones to the wrapped soil is confirmed.

For the sake of completeness, Eq. (15) is rewritten below from Eq. (3) with the strains split into the elastic and plastic parts. Note that by substituting the respective equations for elastic vertical strain ε_a^e, elastic lateral strain ε_r^e, plastic vertical strain increment $\mathrm{d}\varepsilon_a^p$ and plastic lateral strain increment $\mathrm{d}\varepsilon_r^p$ into Eq. (15), the analytical solution for GWS under a given vertical surcharge history is simplified into a problem of solving the nonlinear equation $f(p', \mathrm{d}p', \varepsilon_d) - \sigma_{as} = 0$.

$$\sigma_{as} = K\sigma_r - \frac{2(\sigma_r - \sigma_{rs})(H/B)\left(1 - \varepsilon_a^e - \int \mathrm{d}\varepsilon_a^p\right)}{(H/B+1)\left(1 - \varepsilon_r^e - \int \mathrm{d}\varepsilon_r^p\right)} \tag{15}$$

$$\varepsilon_h = \frac{(\sigma_r - \sigma_{rs})(H/B)\left(1 - \varepsilon_a^e - \int \mathrm{d}\varepsilon_r^p\right)\left(1 - \varepsilon_r^e - \int \mathrm{d}\varepsilon_r^p\right)}{2J(H/B+1)} \tag{16}$$

ε_d is involved in the calculation of $M_f - q/p'$, which is given by Eq. (4) and used later for predicting K_ψ. The integrations of the plastic strain increments $\mathrm{d}\varepsilon_a^p$ and $\mathrm{d}\varepsilon_r^p$ have to be performed numerically, assuming that p' and ε_d remain unchanged at each infinitesimally small loading increment. Hence, all the incremental stress and strain variables and the aforementioned material parameters can be expressed in terms of $\mathrm{d}p'$ at the infinitesimal increase of σ_{as}. In this way, the nonlinear equation with $\mathrm{d}p'$ as the only variable can be solved numerically using an appropriate root finding algorithm. The predicted $\mathrm{d}p'$ and p' are then returned into Eqs. (6), (7) and (13) to update the elastic and plastic strains. Prior to solving $\mathrm{d}p'$ at each increment of σ_{as}, the material parameters K, K' and K_ψ need to be revised from the preceding stress and strain levels. To obtain the evolution of the tensile strain ε_h along the geotextile hoops, Eq. (1) is rewritten as Eq. (16) considering $t_h = J\varepsilon_h$. As the surcharge level increases incrementally, the tensile stress t_h can be computed from the stresses and strains in the wrapped soil until ε_h reaches the maximum value, as illustrated in Fig. 2. The integration will then stop, having the ultimate bearing capacity and the final settlement predicted for the Toyoura sand-filled geotextile container.

4. Model validity

In engineering applications of GWS, initial compaction is typically conducted on assemblies of sand-filled containers to obtain an initial compressive strength (Matsuoka and Liu, 2006). Gaps between neighboring containers are either left empty or filled with loose sand to facilitate the compaction process. Rather than being empirically evaluated from the compactness, the initial strength can be predicted using the proposed analytical solution for GWS considering the designated initial settlement and lateral spreading of the sand-filled containers. To test the validity of the proposed analytical solution for GWS, the macroscopic responses of the DE-GWS model and the AN-GWS model under uniaxial compression loading conditions are compared considering the aforementioned geotextiles (denoted as PE, 0.5PP, PP, 2PP, 3PP and 4PP). The DEM simulations are performed quasi-statically, whereas the analytical predictions are delivered as the compression loading proceeds incrementally.

The geotextile tensile behavior is assumed to be purely elastic in the analytical model with the secant stiffness taken as $J = 53$, 116, 232, 464, 696 and 928 kN/m, whereas the nonlinearity in the tensile behavior is rigorously considered in the DEM simulations. Note that the wide-width tensile strength of PP woven geotextiles generally does not exceed 124.8 kN/m (4PP geotextile). Encapsulating granular soils by high-strength geotextile (e.g., $J >$ 124.8 kN/m) can induce large additional confining pressure onto the soil, when subjected to either compression or shear. The additional confining pressure can be so large that it can cause particle crushing. Because the DE-GWS model cannot reproduce the crushing behavior, only the above-mentioned six geotextiles are chosen for performing the DEM analysis in a physically valid manner. Furthermore, the above range of tensile stiffnesses should be sufficient for demonstrating the applicability of the proposed analytical model in the engineering design of GWS-reinforced foundations. In the DEM simulations, the average tensile stress in the geotextile fabrics at the global failure of the GWS reached approximately half of the effective tensile strength. According to the discussions on the failure evolution of the geotextile fabrics in Cheng et al. (2016), this underestimation resulted from the limitation of discretizing the thin geotextile (0.39 mm thickness) using relatively large spherical particles with a diameter of 5 mm (Fig. 1(c)). Although refining the discretization will certainly improve the agreement with the test results, the DEM predictions from which the current analytical solution is developed are employed in the following for direct comparisons between the results of the analytical and DEM models. Therefore, the tensile strengths of all the geotextiles considered in the AN-GWS model are scaled by a factor of 0.5 to account for the underestimated average tensile strengths that occurred in those DEM simulations.

Fig. 15 shows the relationships between vertical surcharge pressure on the sand-filled container σ_{as} and total vertical strain ε_a obtained from the analytical and DEM models of GWS, considering different values for the geotextile tensile stiffness. An additional experimental response of the surcharge load (partially cyclic) applied on a sand-filled PE geotextile container is provided in Fig. 15(a) to demonstrate the validity of the analytical model. Because it is difficult to measure the area of the top surface as it expands during the experiments, the stresses are calculated as the load Q divided by the reference area $A_0 = 0.16$ to plot the analytical, DEM and experimental stress–strain curves in Fig. 15(a). In the experiments, the sand-filled container underwent an initial compaction stage, which is omitted in the DEM simulations to reduce the computational cost and is thus not present in the analytical model. The dynamic compaction hardens the initial stress–strain behavior of the wrapped soil, causing little difference

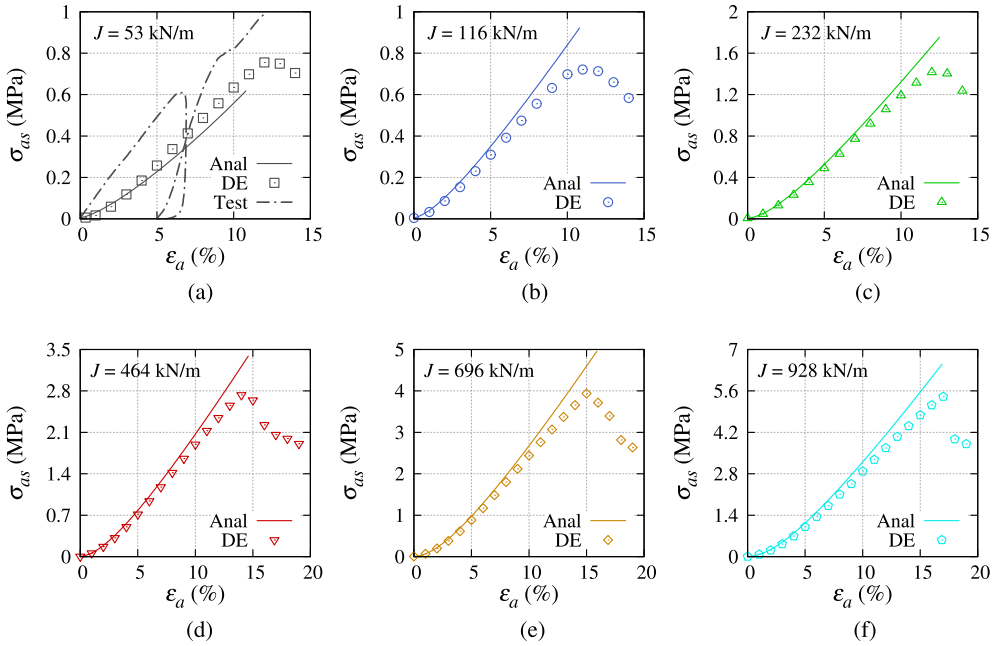

Fig. 15. Comparison of vertical surcharge–strain relationships predicted by the analytical and DEM models of granular soil wrapped by (a) PE, (b) 0.5PP, (c) PP, (d) 2PP, (e) 3PP and (f) 4PP geotextiles.

between the experimental data and the analytical and DEM predictions. Nevertheless, upon truncating the initial soft region of the predicted stress–strain curves, one can observe good agreement among the DEM, analytical and experimental results, i.e., the slopes of all the curves are almost identical (excluding the unloading–reloading path) after ε_a exceeds 4%.

Note that although the compression in Fig. 15 involves large deformation up to approximately 15%, the loading rate is excluded from the stress–strain formulation of the wrapped soil. This simplification is valid because the data for developing the key assumptions in Section 3.1 are extracted from DEM simulations under quasi-static compression. Notwithstanding the simplicity, all the analytical solutions are in very good agreement with the DEM simulation results, regardless of the tensile stiffness. Notably, the initial stiffness increase of the wrapped soil is well reproduced by the proposed analytical model, as shown from all the stress–strain curves in Fig. 15. Because the nonlinearity of the geotextile tensile behavior is ignored in the AN-GWS model, the ultimate bearing capacities obtained from the two approaches are not exactly the same. To reduce this discrepancy, it is feasible to replace the material constant J with a detailed description of the tensile behavior, as shown in Fig. 2, and thus update E in Eq. (9) according to Fig. 14 to introduce greater material nonlinearity. However, this paper avoids this complexity by keeping J constant because the focus is placed on the mechanical behavior of the wrapped soil, e.g., the effects of J on the internal stress–strain behavior as described in the following section. Despite the aforementioned deficiency, the analytical and DEM models are able to produce similar final settlements, which are found to increase as the wrapping geotextile becomes stronger.

4.1. Stress–strain relation of wrapped soil

The internal stress–strain behavior of the wrapped soil and its relation to the tensile strain in the geotextile are of particular interest to the soil–geotextile interaction problems. The previous DEM simulations measured the additional confining pressure applied on the wrapped soil and found that the confinement is evolving toward a more isotropic state during uniaxial compression. Based on the new insights obtained from the DEM analysis in Section 2, the proposed analytical model is capable of accurately predicting the evolutions of the internal stresses, as shown in Fig. 16. Similar to σ_{as} in Fig. 15, the responses of σ_a and σ_r both exhibit an obvious stiffness increase before behaving linearly with respect to ε_a. Comparing the stress levels in Figs. 15 and 16(a), one can confirm the presence of the additional vertical confinement contributed by the geotextile hoops in the lateral planes. Similarly, the additional lateral confinement produced by the hoops in both the lateral and horizontal planes can be understood from Fig. 16(b). Although good agreement is reached between the analytical and DEM solutions for the internal stresses, it is found that the DEM solutions tend to slightly surpass the corresponding analytical solutions in the cases where strong geotextiles are considered.

4.2. Relationship between tensile behavior of geotextile and surcharge pressure on wrapped soil

Analogous to Fig. 8, which displays a unique correlation between tensile stresses and surcharge load regardless of the tensile stiffness of the geotextile, Fig. 16(c) presents a family of straight lines for the analytically obtained relations between tensile strain ε_h and the scaled surcharge pressure σ_{as}/J. J takes the respective geotextile tensile stiffness corresponding to each ε_h–σ_{as} curve. Because a universal tensile stress–strain law is considered for tensile stress along any hoop direction in the analytical model, the DEM solutions for the two tensile strains ε_{ha} and ε_{hr} are averaged for comparison with the analytical solution for ε_h. The analytical model assumes elastic tensile behavior of the geotextile, resulting in linear relationships between ε_h and σ_{as}/J. The DEM model, however, thoroughly considers the nonlinearity of the tensile behavior and thus yields a family of nonlinear ε_h–(σ_{as}/J) curves that lie slightly above the analytical solutions. It is found that the slope of the curve in Fig. 16(c) produced by either the DEM model or the analytical model decreases with increasing geotextile tensile stiffness. It appears that the slopes of the σ_{as}/J–ε_h curves will

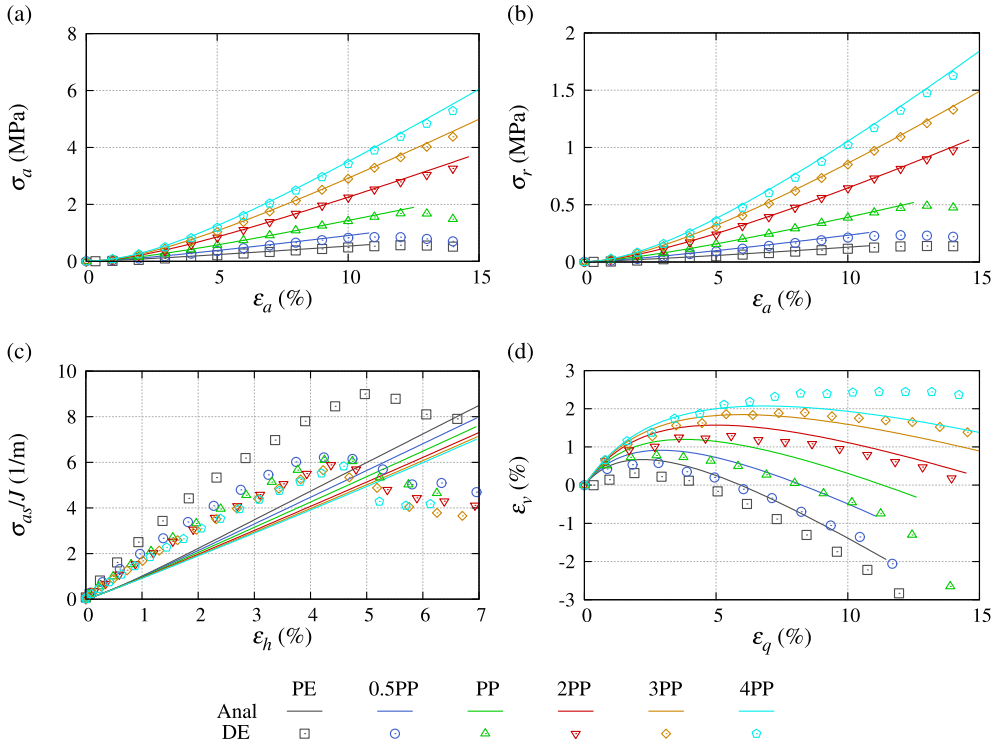

Fig. 16. Comparison of evolutions of internal (a) vertical and (b) lateral stresses versus vertical strain, (c) vertical surcharge pressure scaled with the geotextile tensile stiffnesses versus tensile strain, and (d) volumetric strain versus deviatoric strain.

ultimately converge to a constant after the geotextile tensile stiffness exceeds a sufficiently large value. This trend suggests that wrapping soils with weak geotextiles results in higher efficiency of the reinforcement effect σ_{as}/J than with the strong ones, as long as the geotextile fabrics remain intact. From the perspective of sustainable design of GWS-reinforced foundations, it is of vital importance to balance the reinforcing efficiency, the allowable settlement and the cost for high-strength geotextiles. This comprehensive work could be accomplished with the help of the proposed analytical solution for GWS-like reinforced geomaterials.

4.3. Volumetric deformation

The best agreement between the analytical and DEM solutions for the volumetric response is obtained for the PE case, as shown in Fig. 16(d). As the tensile stiffness of the geotextile increases, the volumetric behavior of the AN-GWS model is predicted to be more increasingly dilative than that in the DEM simulations (see the 3PP and 4PP cases in particular). This is because the assumption of correlating the generalized mean stress $\mathrm{d}p^*$ with the plastic strain increment $\mathrm{d}\varepsilon_a^p$ or $\mathrm{d}\varepsilon_r^p$ via the Young's modulus E (Eq. (13)) does not hold for the strong geotextile cases, as shown in Fig. 13. For the granular soil wrapped within the 2PP, 3PP and 4PP geotextile containers, intercepts could be introduced to fit the DEM simulation data with some linear equations. However, it appears more reasonable to avoid these intercepts by introducing an additional plastic deviatoric strain ε_d^p in the contractive deformation regime and excluding the increments of this ε_d^p from the plastic strain increments used in Fig. 13.

5. Analytical solution for geotextile-wrapped soil in triaxial loading conditions

The assemblies of sand-filled containers are subjected to lateral earth pressures when applied in the construction of retaining walls (Tatsuoka et al., 2007), roads (Matsuoka et al., 2010) and channel slopes (Liu et al., 2015). To examine the predictive capacity of the proposed analytical solution in such loading scenarios, triaxial compression conditions are employed on the AN-GWS model. Although the analytical solution is derived based on a wide range of geotextile tensile stiffnesses, it is still necessary to validate the analytical solution for additional GWS cases in which the geotextile tensile stiffnesses exceed the aforementioned range. Therefore, three types of geotextiles are taken into account: the most commonly used PE and PP geotextiles and a strong geotextile with a tensile stiffness five times greater than that of PP ($J = 1160$ kN/m, denoted as 5PP). The DEM simulations of triaxial loading on GWS are performed by enclosing the DE-GWS model within a periodic cell, as explained in Section 2 and schematically illustrated in Fig. 1(b). Three lateral confining pressures applied from the exterior of the DE-GWS model ($\sigma_{rs} = 10$, 50 and 100 kPa) are considered for the triaxial compression tests. In the DEM simulations, it is straightforward to apply an initial isotropic confining pressure prior to triaxial shearing. In the analytical model, however, p'_0 is assumed to develop from the same initial value as in the uniaxial compression tests ($p'_0 = 2.6$ kPa) rather than starting with the isotropic stress σ_{rs}. This limitation is because the assumptions for the proposed analytical solution are derived based on the stress–strain responses under uniaxial compression. The assumptions stated in Section 3 may not remain valid for triaxial compression conditions. Notably, the assumption of principal stress ratio governed by the NFSL and FSL, although being largely valid during triaxial shearing, cannot consider initial isotropic stress states (Cheng and Yamamoto, 2016). Despite the fundamental difference in the evolution of stress states, the proposed analytical model is employed herein without any assumption pertaining to the triaxial stress–-strain behavior of GWS.

5.1. Surcharge pressure

Despite the aforementioned difference in the initial stress states, the analytical solutions for surcharge pressure on GWS under triaxial compression generally agree with the DEM simulation results, as shown in Fig. 17. The agreement is found to improve as the geotextile tensile stiffness increases because the relations between ε_a and σ_{as} in the cases of stronger geotextiles exhibit more linearity and are less sensitive to confining pressure σ_{rs}, as shown in Fig. 17(b) and (c). Note that this σ_{rs}-sensitive characteristic of GWS can be reproduced by the analytical model, although not as significant as in the DEM simulations (Fig. 18(a)). As the confining pressure increases, both the analytical and DEM solutions provide greater ultimate bearing capacities and final settlements for each GWS. By reducing the tensile strength of each geotextile by two, i.e., using half the strength as explained in Section 4, good agreement is obtained between the analytical and DEM solutions for the final settlements. The ultimate bearing capacity, however, appears to be increasingly overestimated by the analytical model as the geotextile tensile stiffness increases. This trend arises because σ_{as} in the DEM simulations is averaged in the periodic cells that contain both the enclosed GWS and the surrounding soil particles, whereas the analytical model does not take the surrounding soil into account.

5.2. Internal stresses

The responses of the internal stresses σ_a and σ_r appear to be influenced by confining pressure and geotextile tensile stiffness in a similar manner as the responses of σ_{as}. The initial values for the analytical predictions of σ_r are underestimated because p'_0 is assumed to start from 2.6 kPa, which is most distinct in the PE case with a confining pressure of 100 kPa. As the geotextile tensile stiffness increases, better agreement is observed between the analytical and DEM solutions for the σ_r responses (Fig. 19(b)–(c)). Because σ_a is several times larger than σ_r, the initial difference between the σ_a responses predicted by the two solution methods is less significant compared with the σ_r responses, as shown in Figs. 18(a) and Fig. 19(a). Nevertheless, the initial nonlinearity of the σ_a responses in the DEM simulations is not reproduced by the analytical model, as shown in Fig. 18(a). It is known that the stress in wrapped soil under triaxial compression starts from a drained triaxial loading path ($q/p' = 3$), and as the stress level increases, the principal stress ratio gradually evolves toward the values at failure states (Cheng and Yamamoto, 2016). The aforementioned initial nonlinearity of the σ_a responses is a direct result of the evolution of stress ratio with the increase in mean stress. Because the initial stress path is not considered in the proposed analytical model, good agreement with the DEM simulation results cannot be obtained for the soils wrapped by weak geotextiles under triaxial compression. Comparing all the stress–strain responses in Figs. 17–19, one can observe the best agreement between the analytical and DEM solutions for the 5PP case. The assumption of principal stress ratios in Section 3 is sufficiently satisfied for the granular soil wrapped by strong geotextiles. In fact, the additional confining stresses $\sigma_a - \sigma_{as}$ and $\sigma_r - \sigma_{rs}$ in the PE case are only marginal, and the stress state requires more vertical strain to reach the FSL compared with those in the other cases. Despite the initial difference, the responses of σ_a and σ_r obtained from both solution methods are found to eventually obtain similar maximums. Compared with the predictions of ultimate bearing capacities, the differences are less pronounced between the analytical and DEM solutions for the internal stress maximums in Figs. 18 and 19. As the geotextile tensile stiffness increases, it is observed that the analytically predicted maximums of σ_a and σ_r increasingly surpass those in the DEM simulations. This result is primarily attributed to less dilation produced in the analytical model than in the DEM model under triaxial compression, as shown in Fig. 20.

5.3. Volumetric behavior

The volumetric behaviors of the GWS considering PE, PP and 5PP geotextiles under three confining pressures are presented in Fig. 20. The analytical solutions for the volumetric response in the PE case match well with the DEM simulation results. As the geotextile tensile stiffness increases, the proposed analytical solution predicts more contraction than the DEM modeling approach. Regardless of the solution methods, the volumetric behavior tends to become more contractive as both confining pressure and geotextile tensile stiffness increase. The dilation rates of the volumetric responses appear to be unchanged with respect to confining pressure and geotextile tensile stiffness in the DEM simulations under triaxial compression. The analytical predictions of the volumetric behavior, however, show a tendency of decreasing dilation rate with increasing geotextile tensile stiffness. The reason for this tendency is that the proposed analytical solution assumes that the dilation rate is related with the principal stress ratio, which is expected to decrease with increasing mean stress level. To obtain good prediction accuracy in the volumetric behavior, future works are needed to unify the assumptions on the stress states and the stress–dilatancy relations of GWS for both uniaxial and triaxial compression loading conditions.

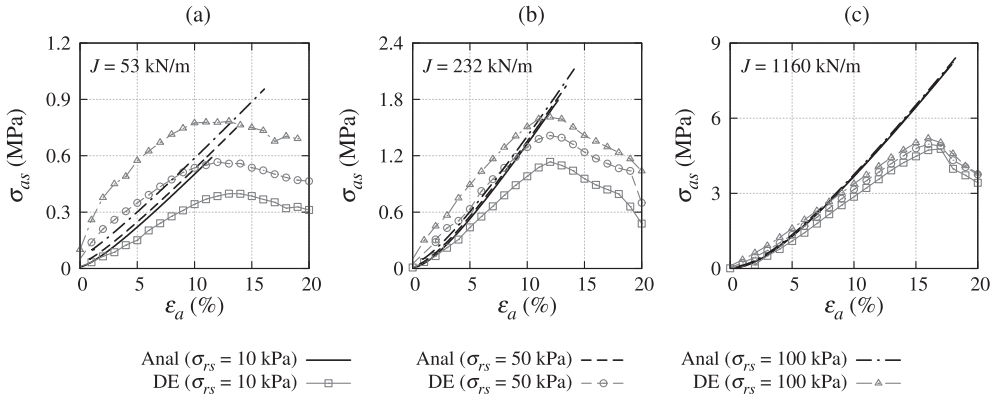

Fig. 17. Comparison of evolutions of vertical surcharge predicted by the analytical and DEM models of granular soil wrapped with (a) PE, (b) PP and (c) 5PP geotextiles.

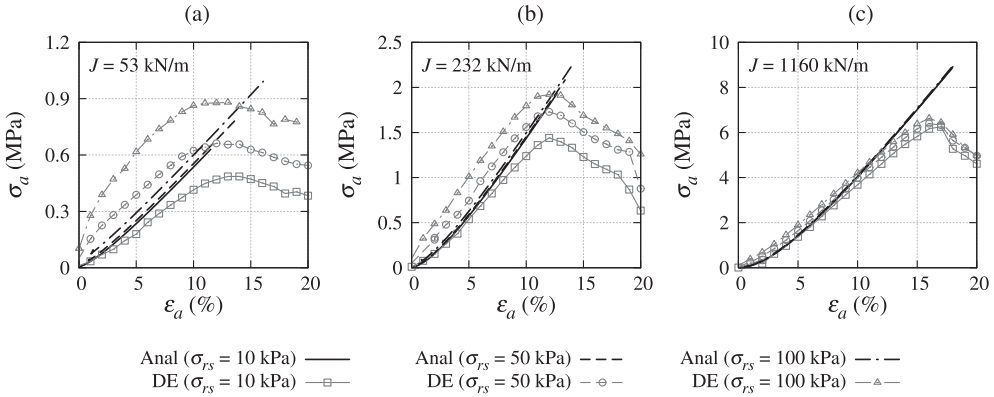

Fig. 18. Evolutions of internal vertical stress predicted by the analytical and DEM models of granular soil wrapped with (a) PE, (b) PP and (c) 5PP geotextiles.

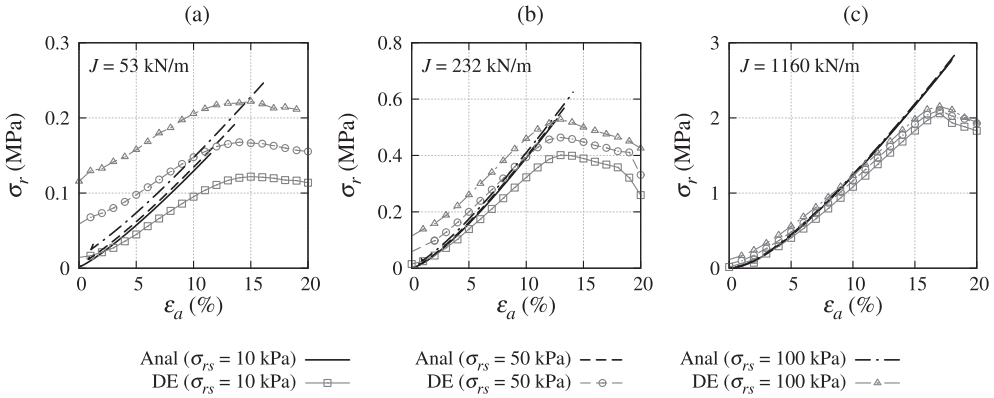

Fig. 19. Comparison of evolutions of internal lateral stress predicted by the analytical and DEM models of granular soil wrapped with (a) PE, (b) PP and (c) 5PP geotextiles.

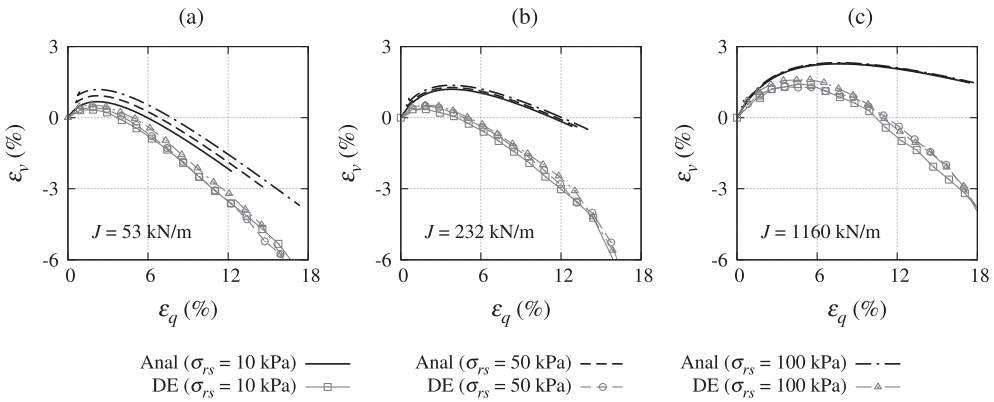

Fig. 20. Comparison of the relationships between deviatoric strain and volumetric strain predicted by the analytical and DEM models of granular soil wrapped with (a) PE, (b) PP and (c) 5PP geotextiles.

6. Conclusions

This paper presents a novel analytical solution for geotextile-wrapped soil in compression loading conditions, with the assumptions facilitated by the new findings obtained from the DEM modeling of a sand-filled container. The analytical model considers the geotextile tensile behavior to be purely elastic and the wrapped soil to be a Mohr–Coulomb elastoplastic solid with evolving principal stress ratio and dilation rate. To examine the boundary and interface assumptions for the proposed analytical model, the principal stress distribution and interface friction are investigated in a DEM analysis of geotextile-wrapped soil under uniaxial and triaxial compression. To obtain a better understanding of the stress–strain behavior of the reinforced soil and its relation to tension in the geotextile fabrics, four additional cases are considered for the uniaxial compression simulations with tensile stiffnesses of half, two, three and four times that of a PP geotextile. The assumptions for the analytical model are made based on the following findings from the DEM analysis:

- *Boundary conditions:* The major principal stress directions remain parallel to the axis of the uniaxial loading. The medium

and minor principal stress directions are slightly inclined toward the corners.

- *Contractive behavior of soil:* The initial contraction of wrapped soil follows the compression line in the semi-log mean stress–void ratio plane without reference to geotextile tensile stiffness.
- *Dilative behavior of soil:* The plastic deformation of the wrapped soil is governed by the Mohr–Coulomb yield criterion with evolving dilation rate and principal stress ratio.
- *Stress ratio:* A unique relationship is identified between deviatoric strain and the relative principal stress ratio with respect to the maximum value at failure state. The failure state lines for soils with or without a cellular form of reinforcement are identical.
- *Dilation rate:* The principal stress ratio and its maximum on the failure line are related to the dilation rate through a linear correlation irrespective of the geotextile tensile stiffness.
- *Tensile behavior of geotextile:* The geotextile behaves as a perfectly elastic material with the same amount of tension developed in every constituent hoop of the geotextile reinforcement.

Because the material parameters need to be updated during compression loading, the analytical solution for geotextile-wrapped soil is solved numerically. By imposing an empirical power-law relation between the geotextile tensile stiffness and the Young's modulus of the wrapped soil, good agreement is obtained between the analytical and DEM solutions for geotextile-wrapped soil in uniaxial loading conditions. The predictive capacity of the proposed analytical solution is further examined in triaxial compression conditions, varying the confining pressure and geotextile tensile stiffness at three different levels. Based on the analytical solutions and comparative DEM simulations, the following conclusions are drawn:

- The analytical solutions for the internal stresses within the reinforced soil and the vertical surcharge applied on the geotextile are in excellent agreement with the DEM solutions regardless of the geotextile tensile stiffness.
- The initial stiffness increase of the geotextile-wrapped soil in the responses of the internal stress and the external surcharge pressure is well reproduced by the analytical model.
- The slope of the straight line that displays the linear relationship between the surcharge pressure and the tensile stress tends to decrease to a constant value as the geotextile tensile stiffness increases. This trend suggests higher reinforcing efficiency in the cases of weak geotextiles. It is recommended that the reinforcing efficiency, the allowable settlements and the costs for high-strength geotextiles should be balanced in the sustainable design of geotextile-wrapped soil with the help of the proposed analytical solution.
- The analytical solutions for the surcharge pressure on geotextile-wrapped soil under triaxial compression generally agree with the DEM solutions. The agreement is found to improve with increasing geotextile tensile stiffness.
- As the confining pressure increases, both the analytical and DEM solutions provide greater ultimate bearing capacities and larger final settlements.
- Although the analytically predicted internal lateral stresses are initially lower than the DEM simulation results, similar maximums of the internal stresses are produced by the analytical and DEM models.
- Because the agreement between the two solutions improves as the geotextile tensile stiffness increases, it is concluded that the assumptions of principal stress ratios still hold for triaxial loading conditions as long as strong geotextiles are considered.
- As the geotextile tensile stiffness increases, the analytical solutions for the volumetric response become less dilative, and larger contraction is predicted compared with the DEM simulation results. Further improvements could be achieved with unified assumptions on the principal stress ratio and dilation rate for geotextile-wrapped soil under both uniaxial and triaxial loading conditions.

Acknowledgments

The financial support of the Graduate School for International Development and Cooperation at Hiroshima University provided to the first author is gratefully acknowledged.

References

Balaam, N., Booker, J., 1985. Effect of stone column yield on settlement of rigid foundations in stabilized clay. Int. J. Numer. Methods Eng. 9 (4), 331–351.
Bhandari, A., Han, J., Parsons, R.L., 2015. Two-dimensional DEM analysis of behavior of geogrid-reinforced uniform granular bases under a vertical cyclic load. Acta Geotech. 10 (4), 469–480.
Chen, C., Indraratna, B., McDowell, G., Rujikiatkamjorn, C., 2015. Discrete element modelling of lateral displacement of a granular assembly under cyclic loading. Comput. Geotech. 69, 474–484.
Cheng, H., Yamamoto, H., 2016. Evaluating the performance of geotextile wrapped/layered soil: a comparative study using the DEM. In: Geo-China 2016. Jinan, China, pp. 122–130.
Cheng, H., Yamamoto, H., Jin, S., Okano, S., 2013. Soil reinforcement using soilbags a preliminary study on its static and dynamic properties. In: Geotech. Sustain. Dev. Hanoi, Vietnam, pp. 569–578.
Cheng, H., Yamamoto, H., Thoeni, K., 2016. Numerical study on stress states and fabric anisotropies in soilbags using the DEM. Comput. Geotech. 76, 170–183.
Effeindzourou, A., Thoeni, K., Giacomini, A., Wendeler, C., 2017. Efficient discrete modelling of composite structures for rockfall protection. Comput. Geotech. 87, 99–114.
Geng, L., Tang, L., Cong, S.Y., Ling, X.Z., Lu, J., 2017. Three-dimensional analysis of geosynthetic-encased granular columns for liquefaction mitigation. Geosynth. Int. 24 (1), 45–59.
Giroud, J.P., Han, J., 2004. Design method for geogrid-reinforced unpaved Roads. II. calibration and applications. J. Geotech. Geoenviron. Eng. 130 (8), 787–797.
Gu, X., Hu, J., Huang, M., 2017. Anisotropy of elasticity and fabric of granular soils. Granul. Matter 19 (2), 33.
Guo, W., Chu, J., Yan, S., Nie, W., 2014. Analytical solutions for geosynthetic tube resting on rigid foundation. Geomech. Eng. 6 (1), 65–77.
Hussein, M., Meguid, M., 2016. A three-dimensional finite element approach for modeling biaxial geogrid with application to geogrid-reinforced soils. Geotext. Geomembranes 44 (3), 295–307.
Koerner, R.M., 2012. Designing with Geosynthetics, sixth ed. Xlibris Corporation.
Kumar, N., Luding, S., Magnanimo, V., 2014. Macroscopic model with anisotropy based on micro-macro information. Acta Mech. 225 (8), 2319–2343.
Lai, H.-J., Zheng, J.-J., Zhang, J., Zhang, R.-J., Cui, L., 2014. DEM analysis of soil-arching within geogrid-reinforced and unreinforced pile-supported embankments. Comput. Geotech. 61, 13–23.
Latha, G.M., Murthy, V.S., 2007. Effects of reinforcement form on the behavior of geosynthetic reinforced sand. Geotext. Geomembr. 25 (1), 23–32.
Liu, S., Lu, Y., Weng, L., Bai, F., 2015. Field study of treatment for expansive soil/rock channel slope with soilbags. Geotext. Geomembr. 43 (4), 283–292.
Magnanimo, V., La Ragione, L., 2013. A micromechanical numerical analysis for a triaxial compression of granular materials. AIP Conf. Proc. 1542 (1), 1234–1237.
Matsuoka, H., Liu, S., 2003. New earth reinforcement method by soilbags ("Donow"). Soils Found. 43 (6), 173–188.
Matsuoka, H., Liu, S., 2006. A New Earth Reinforcement Method Using Soilbags. Taylor & Francis/Balkema, The Netherlands.
Matsuoka, H., Liu, S., Hasebe, T., Shimao, R., 2004. Deformation-strength properties and design methods of soilbag assembly. Dob. Gakkai Ronbunshu 764 (III-67), 169–181.
Matsuoka, H., Yamamoto, H., Nomoto, F., 2010. D·Box method as modern soilbag technology and its local consolidation and vibration reduction effects. Geosynth. Eng. J. 25, 19–26.
Muramatsu, D., Bin, Y., Zhang, F., 2009. Numerical simulation of vibration damping effect of soilbag. Jpn. Geotech. J. 4 (1), 71–80.
Ngo, N.T., Indraratna, B., Rujikiatkamjorn, C., Biabani, M.M., Mahdi Biabani, M., 2015. Experimental and discrete element modeling of geocell-stabilized subballast subjected to cyclic loading. J. Geotech. Geoenviron. Eng. 04015100.
Oliaei, M., Kouzegaran, S., 2017. Efficiency of cellular geosynthetics for foundation reinforcement. Geotext. Geomembr. 45 (2), 11–22.
O'Sullivan, C., 2011. Particulate Discrete Element Modelling: a Geomechanics

Perspective. Taylor & Francis, Hoboken, NJ.
Palmeira, E.M., 2009. Soil–geosynthetic interaction: modelling and analysis. Geotext. Geomembr. 27 (5), 368–390.
Pulko, B., Majes, B., Logar, J., 2011. Geosynthetic-encased stone columns: analytical calculation model. Geotext. Geomembr. 29 (1), 29–39.
Rowe, R.K., Skinner, G.D., 2001. Numerical analysis of geosynthetic reinforced retaining wall constructed on a layered soil foundation. Geotext. Geomembr. 19 (7), 387–412.
Šmilauer, V., et al., 2015. Using and Programming. In: Yade Documentation 2nd ed. The Yade Project, http://yade-dem.org/doc/.
Sukmak, K., Han, J., Sukmak, P., Horpibulsuk, S., 2016. Numerical parametric study on behavior of bearing reinforcement earth walls with different backfill material properties. Geosynth. Int. 23 (6), 435–451.
Sun, D., Huang, W., Sheng, D., Yamamoto, H., 2007. An elastoplastic model for granular materials exhibiting particle crushing. Key Eng. Mater 340–341, 1273–1278.
Tafreshi, S.M., Dawson, A., 2010. Comparison of bearing capacity of a strip footing on sand with geocell and with planar forms of geotextile reinforcement. Geotext. Geomembr. 28 (1), 72–84.
Tantono, S.F., 2007. The Mechanical Behavior of a Soilbag under Vertical Compression. Ph.D. thesis. Graz University of Technology.
Tatsuoka, F., Tateyama, M., Mohri, Y., Matsushima, K., 2007. Remedial treatment of soil structures using geosynthetic-reinforcing technology. Geotext. Geomembr. 25 (4–5), 204–220.
Thoeni, K., Lambert, C., Giacomini, A., Sloan, S.W., 2013. Discrete modelling of hexagonal wire meshes with a stochastically distorted contact model. Comput. Geotech. 49, 158–169.
Thoeni, K., Giacomini, A., Lambert, C., Sloan, S.W., Carter, J.P., 2014. A 3D discrete element modelling approach for rockfall analysis with drapery systems. Comput. Geotech. 68, 107–119.
Thornton, C., Cummins, S.J., Cleary, P.W., 2011. An investigation of the comparative behaviour of alternative contact force models during elastic collisions. Powder Technol. 210 (3), 189–197.
Wang, L.-J., Liu, S.-H., Zhou, B., 2015. Experimental study on the inclusion of soilbags in retaining walls constructed in expansive soils. Geotext. Geomembr. 43 (1), 89–96.
Wang, Z., Jacobs, F., Ziegler, M., 2016. Experimental and DEM investigation of geogrid–soil interaction under pullout loads. Geotext. Geomembr. 44 (3), 230–246.
Wu, C.-S., Hong, Y.-S., 2014. A simplified approach for evaluating the bearing performance of encased granular columns. Geotext. Geomembr. 42 (4), 339–347.
Wu, Y., Yamamoto, H., Yao, Y., 2013. Numerical study on bearing behavior of pile considering sand particle crushing. Geomech. Eng. 5 (3), 241–261.
Wu, Y., Yoshimoto, N., Hyodo, M., Nakata, Y., 2014. Evaluation of crushing stress at critical state of granulated coal ash in triaxial test. Géotech. Lett. 4 (4), 337–342.
Xu, Y., Huang, J., Du, Y., Sun, D., 2008. Earth reinforcement using soilbags. Geotext. Geomembr. 26 (3), 279–289.
Yao, Y.-P., Yamamoto, H., Wang, N.-D., 2008. Constitutive model considering sand crushing. Soils Found. 48 (4), 603–608.